Title

Automated Breast Density Measurements From Chest Computed Tomography Scans.

Journal

Journal of Medical Systems, 43(8)

Authors

Qureshi, Touseef
Veeraraghavan, Harini
Sung, Janice
et al.

Publication Date

2019-06-22

DOI

10.1007/s10916-019-1363-9

Peer reviewed

Published in final edited form as:

J Med Syst. ; 43(8): 242. doi:10.1007/s10916-019-1363-9.

Automated Breast Density Measurements From Chest Computed Tomography Scans

Touseef A. Qureshi,
Cedars-Sinai Medical Center, Biomedical Imaging Research Institute, 8700 Beverly Blvd, Pact 400, Los Angeles, CA, 90048

Harini Veeraraghavan,
Memorial Sloan Kettering Cancer Center, Department of Medical Physics, 485 Lexington Avenue, New York, NY 10017

Janice S. Sung,
Memorial Sloan Kettering Cancer Center, Department of Radiology, 1275 York Avenue, New York, NY 10065

Jennifer B. Kaplan,
Memorial Sloan Kettering Cancer Center, Department of Radiology, 1275 York Avenue, New York, NY 10065

Jessica Flynn,
Memorial Sloan Kettering Cancer Center, Department of Epidemiology and Biostatistics, 485 Lexington Avenue, New York, NY 10017

Emily S. Tonorezos,
Memorial Sloan Kettering Cancer Center, Department of Medicine, 485 Lexington Avenue, New York, NY

Suzanne L. Wolden,
Memorial Sloan Kettering Cancer Center, Department of Radiation Oncology, 1275 York Avenue, New York, NY 10065

Elizabeth A. Morris,
Memorial Sloan Kettering Cancer Center, Department of Radiology, 1275 York Avenue, New York, NY 10065

Kevin C. Oeffinger,

Corresponding author: Chaya S. Moskowitz, Ph.D., Department of Epidemiology and Biostatistics, Memorial Sloan Kettering Cancer Center, 485 Lexington Avenue, 2nd Floor, New York, NY 10017, moskowc1@mskcc.org, Phone: 646-888-8232.

Ethical approval

This study used archived images and does not contain any studies with humans or animals performed by any of the authors.

Informed consent

Informed consent was waived by our institutional review board.

Duke University, Department of Medicine, 2424 Erwin Dr, Suite 601, Durham, NC 27705

Malcolm C. Pike,
Memorial Sloan Kettering Cancer Center, Department of Epidemiology and Biostatistics, 485 Lexington Avenue, New York, NY 10017

Chaya S. Moskowitz
Memorial Sloan Kettering Cancer Center, Department of Epidemiology and Biostatistics, 485 Lexington Avenue, New York, NY 10017

Abstract

Objectives: To develop an automated method for quantifying percent breast density from chest computed tomography (CT) scans.

Methods: A naïve Bayesian classifier based on gray-level intensities and spatial relationships was developed on CT scans from 10 patients diagnosed with Hodgkin lymphoma (HL) and imaged as part of routine clinical care. The algorithm was validated on CT scans from 75 additional HL patients. The classifier was developed and validated using a reference dataset with consensus manual segmentation of fibroglandular tissue. Accuracy was evaluated at the pixel-level to examine how well the algorithm identified pixels with fibroglandular tissue using true and false positive fractions (TPF and FPF, respectively). Quantitative estimates of the patient-level CT percent density were contrasted to each other using the concordance correlation coefficient, ρ_c, and to subjective ACR BI-RADS density assessments using Kendall's τ_b.

Results: The pixel-level TPF for identifying pixels with fibroglandular tissue was 82.7% (interquartile range of patient-specific TPFs 65.5%-89.6%). The pixel-level FPF was 9.2% (interquartile range of patient-specific FPFs 2.5%-45.3%). Patient-level agreement of the algorithm's automated density estimate with that obtained from the reference dataset was high, ρ_c =0.93 (95% CI 0.90-0.96) as was agreement with a radiologists' subjective ACR-BI-RADS assessments, τ_b =0.77.

Conclusions: It is possible to obtain automated measurements of percent density from clinical CT scans.

Keywords

algorithm; Bayes theorem; breast density; risk

Fibroglandular tissue in the breast is most frequently visualized with mammography due to the widespread use of mammography as a screening test. Because it is denser than the fatty components of the breast, fibroglandular tissue appears as a white area on a mammogram. The amount of fibroglandular breast tissue seen on a mammogram, referred to as mammographic breast density, is an established major breast cancer risk factor; higher breast density is associated with an increased risk of breast cancer [1; 2]. Recent work suggests fibroglandular breast tissue is seen not only with mammography, but also with other imaging modalities including digital breast tomosynthesis [3], dual-energy x-ray imaging [4], magnetic resonance imaging [5], optical imaging modalities [6], and computed tomography (CT) [7].

The ability to assess breast density from CT scans is particularly intriguing. CT has been used ubiquitously to diagnose, stage, and follow patients diagnosed with a variety of cancers including pediatric and young adult cancers. Clinical chest CT scans stored in institutional imaging archiving systems provide an opportunity to explore breast composition at young ages when assessing mammographic breast density is not feasible. With the multitude of scans available for analysis, it would be beneficial to have a method that automates quantifying breast density from CT scans.

There have been several computational methods proposed for quantifying breast density from CT scans. Most methods are semi-automated and require user-involvement to help select the breast region [8–11]. Segmentation of the breast is most frequently accomplished using one of several histogram thresholding methods to classify areas based on Hounsfield units [8; 12], but has also been attempted using fuzzy C means clustering [9]. Because distributions of CT gray level intensities for fibroglandular tissue and non-fibroglandular structures such as pectoral muscle substantially overlap, threshold-based methods may result in erroneous classification of fibroglandular tissue. Additionally, semi-automated methods such as methods requiring users to mark the breast area on individual CT slices are very time-consuming and subject to inter-rater variability.

Here we describe a fully automated approach that uses a supervised Bayesian probabilistic model. The algorithm sequentially identifies the lungs, heart, and pectoral muscle using CT intensities and spatial contextual information to isolate the breast region and then segment it into fibroglandular tissue and fat from three-dimensional chest CT data.

Materials and Methods

Datasets

This study used 85 chest CT scans obtained 1996-2012 during routine care of female patients diagnosed with Hodgkin lymphoma (HL) at a wide range of ages. Median age at the CT scan was 35 years (interquartile range (IQR) 30-43 years). Informed consent was waived by our institutional review board.

Scans were performed with a number of GE Medical System scanners routinely used at our institution. Imaging acquisition parameters varied; details are provided in the online supplementary material. The median number of breast slices per patient was 16 (range 7-23 slices). The resolution of the cross-sectional slices was approximately 368 x 512 pixels. Pixel intensities for each scan were scaled to lie within the range of [0, 1].

Ten CT scans (age at scan ranging from 22 to 42 years) were initially used to train the algorithm. The remaining 75 scans were used for validation.

A ground-truth reference dataset was created for each of the 85 scans. This dataset contained detailed annotations of the anatomical structures necessary to train the algorithm and all areas of fibroglandular tissue in the breast region. All labeling was determined by two individuals working together and reviewed by one of two breast imaging radiologists with 16 and 9 years of experience including expertise evaluating CT scans. The dataset was

converted to a pixel-level reference dataset labeling whether individual pixels corresponded to fibroglandular tissue.

Among the 75 validation scans, 45 CT scans were acquired with 6 months of a mammogram. Blinded to clinical data, a single radiologist evaluated these 45 CT scans using the Breast Imaging Reporting and Data System of the American College of Radiology (ACR BI-RADS) breast density categories [13] reflecting how radiologists might interpret a scan in practice. In a different random order separated by a period of time, she also assessed breast density from the mammograms. A second radiologist independently assessed ACR BI-RADS breast density from both CT scans and mammograms to characterize inter-reader variability.

Method overview

The system (Figure 1) follows a hierarchical, tree-based approach. This approach, used in other applications to segment medical images [14], sequentially eliminates regions in separate phases using results of each phase to narrow down the search for the breast region. Fibroglandular tissue is ultimately identified by eliminating the fatty portion of the breast.

The analysis is performed slice-by-slice and classifies pixels into regions using a supervised naïve Bayes classifier. Different classifiers are used for individual phases, including a chest classifier in Phase 1, lung detector in Phase 2, pectoral muscle detector in Phase 3, and finally fibroglandular tissue detector in Phase 4.

Let x_i denote the i^{th} pixel. We represent the anatomical structure of interest as S and the remaining image area that does not include this structure as $\acute{S}$. The set of features, f, which varies based on the phase, is used to segment pixels using the conditional probability model

$$p(x_i \in S \mid f) = \frac{p(f \mid x_i \in S)p(x_i \in S)}{p(f \mid x_i \in S)p(x_i \in S) + p(f \mid x_i \in \acute{S})p(x_i \in \acute{S})} \quad (1)$$

where p represents a probability density function. We use non-informative prior probabilities ($p(x_i \in S)$) of 0.5. The maximum a posteriori parameter estimates are used to construct decision rules. In each phase pixels are assigned to the class with the highest posterior probability. Below we give further details specific to each phase.

Identification of the lungs, heart, and chest wall

After the background (air) is removed from the entire image, the system first segments and eliminates the lungs. f consists only of the gray level intensities, v, in Phase I. We assume a Gaussian distribution and derived maximum likelihood estimates from the training data for the mean, μ=0.12, and standard deviation, σ=0.10, of this distribution. In Phase 2 structures near the lung, including the chest wall, heart, and posterior chest area but excluding the pectoral muscle, are removed. This is accomplished by constructing a horizontal boundary that approximately separates the breast and pectoral muscle from the rest of the two-dimensional image (Figure 2). Because lung and posterior chest size and position within the two-dimensional image vary, we determined placement of this boundary considering both factors. Let y_1 and y_2 be y-axis coordinates of the top-left and right corner pixels of the left

lung and y_3 and y_4 represent coordinates of the top-left and right corner pixels of the right lung. Similarly, y_5, …, y_8 are y-axis coordinates of the bottom left-most and right-most pixels in the left and right lungs, respectively. The horizontal boundary, B, is ¼ the approximate average vertical length of the lungs, $B = \frac{1}{4}\left(\frac{\sum_{i=5}^{8} y_i}{4} - \frac{\sum_{i=1}^{4} y_i}{4}\right)$. All pixels below B are removed from further consideration.

Elimination of the pectoral muscle

This task is relatively difficult because of substantial overlap of the pixel gray level intensity distributions of fibroglandular tissue and pectoral muscle (seen in Figures 2 and 3 where fibroglandular tissue and pectoral muscle look similar with respect to their intensities). In addition, fibroglandular tissue and pectoral muscle share boundaries complicating the classification task. To overcome this difficulty, our system uses information on the spatial relationship between fibroglandular tissue and pectoral muscle.

Allowing for images with different resolutions when utilizing information on spatial relationships within an image, we first calculate the height of the entire chest area (removing the background) by taking the difference, h, between the y-axis coordinates of the two pixels on the boundary of the chest with the highest and lowest y-axis coordinates. Define distance offset, d', as the Euclidean distance between a pixel and the nearest pixel on the boundary with the lungs. Conceptually, small values suggest pixels belonging to pectoral muscle while large values suggest pixels belonging to the breast (Figure 3a). The algorithm uses this distance offset relative to the chest area height, $d=d'/h$, to segment pectoral muscle where both h and d' were estimated for each patient (Figure 3b).

The feature vector f now consists of two features, the gray level intensity, v, and the relative distance offset, d. We assume these features are statistically independent and both have a Gaussian distribution; thus, the joint posterior probability is $p(x_i \in S | f = (v, d)) = p(x_i \in S \mid f = (v)) \times p(x_i \in S \mid f = (d))$. From the training data, the maximum likelihood estimates of the mean and standard deviation of the distribution of d were μ=0.024 and σ=0.022, respectively; for the distribution of v in this phase they were μ=0.78 and σ=0.28, respectively.

Segmenting fibroglandular tissue and estimating CT breast density

After Phases 1-3, the remaining area is comprised predominantly of breast tissue. The leftmost and rightmost pixels of the breast on the horizontal axis are identified and the difference between these points taken as the width of the breast region. The middle 5% of this length, corresponding to the sternum, is removed from the breast region.

Lastly, the outer edges of the breast image appear hyper-intense with a bright thin region along the breasts' outer boundary. This skin region is eliminated by using morphological erosion with a filter with a diameter of 5 pixels along each axis (or a 5x5 filter).

The final phase identifies fibroglandular tissue in the defined breast region and separates it from the fatty part of the breast. In this phase, the feature set f consists only of the gray level intensities, v.

With fgt equal to the number of pixels identified as fibroglandular tissue, $non\text{-}fgt$ equal to the number of breast pixels not identified as fibroglandular tissue, and T equal to the total number of breast region pixels (i.e. $T = fgt + non\text{-}fgt$), percent density is estimated as $D = fgt/T$.

Statistical Methods

Pixel-level accuracy of fibroglandular tissue segmentation in the validation dataset was evaluated by comparing assessments from the algorithm and labeled reference dataset within the breast region identified by the algorithm. True positive pixels were pixels identified as fibroglandular tissue by both the algorithm and the reference dataset and false positive pixels were pixels identified as fibroglandular tissue by the algorithm but not the reference dataset. We quantified pixel-level accuracy using true and false positive fractions (TPF and FPF, respectively) together with 95% confidence intervals reflecting the correlation between multiple pixels in the same patient [15].

Agreement between the algorithm's CT percent density and the reference dataset's CT percent density was evaluated using the concordance correlation coefficient (ρ_c, [16]) and Bland-Altman plots [17], Kendall's τ_b was used to evaluate correlation of the categorical subjective BI-RADS assessments and the continuous algorithm's density measurements, and a weighted kappa with quadratic weights [18] was used to assess inter-reader variability for categorical ACR BI-RADS assessments.

Results

The algorithm was able to automatically remove the lungs, heart, and muscles in all 75 testing patients satisfactorily as illustrated in Figures 4 and 5.

Pixel-level accuracy

The pixel-level TPF for identifying pixels with fibroglandular tissue was 82.7% (IQR of patient-specific TPFs 65.5%-89.6%). The pixel-level FPF was 9.2% (IQR of patient-specific FPFs 2.5%-45.3%). Overall accuracy was 87.1%.

Agreement in quantitative density estimates

There was very good agreement between percent density estimated from the algorithm and percent density estimated from the reference labeled dataset, ρ_c =0.93 (95% CI 0.90-0.96). Median percent density estimated from the algorithm was 23% (IQR 14%-45%) and median percent density estimated from the reference labeled dataset was 18% (IQR 8%-38%).

The algorithm tended to overestimate percent density particularly in cases with small values corresponding to breasts with little-to-no fibroglandular tissue. The largest differences were seen in pre-pubescent females with thin breast regions where the algorithm incorrectly identified pectoral muscle as fibroglandular tissue. Figure 5 shows differences between

density estimated from the algorithm and density estimated from the reference dataset. In cases where the reference breast density was greater than 5% (Figure 5(b)), the average ratio of the algorithm's density measurement relative to the reference data density measurement was 1.2.

Agreement with subjective BI-RADS assessments

For the 45 patients with mammograms within six months of CT scans, there was very good within-reader agreement between subjective density assessments made on the chest CTs and mammograms (Table 1 and Figure 6).

In these patients, median CT density from the algorithm was 20% (IQR 7%-40%). Figure 6A shows the automated CT density estimate plotted against the radiologist's subjective ACR BI-RADS assessment. There was good correlation between quantitative CT density estimates and radiologist's assessment, although the ranges of the quantitative values overlap particularly for the middle ACR BI-RADS categories.

We explored two additional ways of estimating CT density from the algorithm's segmentation results. First, we limited the number of slices contributing to the estimate by identifying the slice with the maximum CT density and taking five slices above and below it for a total of 11 breast slices. For patients with less than 11 breast slices, we used all slices (Figure 6B). Second, we explored using only the slice with the maximum CT density (Figure 6C). The range of quantitative values within ACR BI-RADS categories overlap slightly less for the limited slices approach although differences are small. τ_b was 0.77 in all three instances. As noted above, Figure 6D and Table 1 show that there is some variation between readers in subjective assessments as well.

Discussion

The computational algorithm we describe here is a novel method for automatically quantifying breast density from chest CT scans obtained as part of standard clinical care for patients for whom the breast was not the imaging test's focus. Using a naïve Bayesian classifier with CT intensities and spatial constraints, we successfully detected the breast region and estimated the percent of the breast that contained fibroglandular tissue without any user-involvement.

Glandular and fibrous tissues are two of several structural components of the breast. With the ubiquitous use of mammography for breast cancer screening and diagnosis, most of the work studying the association between fibroglandular tissue and breast cancer risk has assessed fibroglandular tissue in the breast from mammography images. The more fibroglandular tissue seen on a mammographic image, the greater the risk of breast cancer regardless of a women's age or menopausal status [2; 19]. This relationship holds when mammographic density is assessed qualitatively using a subjective classification system such as BI-RADS or quantitatively using a continuous measurement, such as the percentage of the mammogram with radiodense fibroglandular tissue [2; 20].

Both mammography and CT use x-rays to generate images. CT breast density is simply another way to measure the same structural components from a different imaging test. While it seems reasonable to infer that breast density assessed on CT scans is a risk factor for breast cancer, studies explicitly evaluating this association are limited. To our knowledge there is one relevant case-control study. Kuchiki, Hosoya, and Fukao assess the relationship between volume of fibroglandular tissue measured from chest CTs and breast cancer risk [21]. They found that women with breast cancer had significantly higher fibroglandular tissue volumes than age-matched women without breast cancer. As with mammographic breast density, this relationship held regardless of menopausal status. In their study, however, the breast region was manually identified.

Automated image analysis of CT scans for assessing breast density has multiple benefits. First, in the last decade there have been several studies studying breast-tissue composition in young women in order to understand how breast density develops [4; 22; 23]. These studies have been hampered by relatively small sample sizes resulting from the need to conduct prospective studies using breast imaging modalities other than mammography (to avoid radiation exposure). In contrast, CT is often used as a diagnostic and treatment planning tool in pediatric and young adult patients; digitally stored images provide a rich repository for retrospective analyses. Second, by automating the process, large numbers of images can be analyzed with minimal time commitments from radiologists [24; 25]. Third, as with any automated image analysis application, there is potential for the subjectivity and resulting variability (arising from both intra- and inter-reader variability) associated with reader-involvement to be reduced [24; 25].

There are several limitations of our study worth noting. As described above, the algorithm did not do as well in younger females where the breast region was thin. The training set consisted of images of females 22-42 years old. To understand how the algorithm worked in a broader population, we did not restrict the age range of the testing set. However, we suspect there is little interest in quantifying breast density of pre-pubescent females and do not view the difficulty the algorithm had in these few cases as a major limitation. Second, the presented results suggest a tendency for the algorithm to slightly overestimate percent density. Our primary focus was on characterizing the algorithm’s accuracy identifying fibroglandular tissue. Consequently, we compared the percent of fibroglandular tissue identified by the algorithm and the reference dataset relative to the total breast region defined by the algorithm. While useful for looking at pixel-level accuracy, this may contribute to the differences observed in patient-level percent density. Third, the distributions of the quantitative CT density measurement overlapped across the radiologist’s subjective ACR BI-RADS categories.

Although we used assessments from an experienced breast imaging radiologist also trained in CT body imaging for comparison, we expect variability just as there is variability in ACR BI-RADS density assessments obtained from reading mammograms [26]. Here we found good, but not perfect, agreement between subjective readings performed by different radiologists. Fourth, the algorithm assumes a consistent range of intensities across scans. If this is not the case, we recommend using an available method for contrast correction [27]. Finally, we used data from a single institution with all scans obtained from GE scanners to

train and validate the algorithm. The scanner models and imaging acquisition parameters varied reflecting scans obtained in clinical practice allowing our results to have some degree of generalizability. However, we leave studying reproducibility of the algorithm for future work.

In conclusion, our algorithm performed well at identifying breast regions from chest CT scans with no user-input. Importantly, it estimated percent breast density with a high degree of accuracy in most cases.

Supplementary Material

Refer to Web version on PubMed Central for supplementary material.

Acknowledgments

Funding Information

Funding for this work came from the Meg Berté Owen Foundation and from NCI grant P30 CA008748.

Conflict of interests

TA Qureshi, H Veeraraghavan, JB Kaplan, J Flynn, ES Tonorezos, KC Oeffinger, MC Pike, and CS Moskowitz declare no conflicts of interest. JS Sung has received research grants from Hologic and GE. SL Wolden has received honoraria from YmAbs. EA Morris has received research grants from GRAIL.

Abbreviations

ACR	American College of Radiology
BI-RADS	Breast Imaging Reporting and Data System
CT	Computed Tomography
FPF	False positive fraction
GE	General Electric
HL	Hodgkin lymphoma
IQR	Interquartile range
TPF	True positive fraction

References

1. Boyd NF, Guo H, Martin LJ et al. (2007) Mammographic density and the risk and detection of breast cancer. N Engl J Med 356:227–236 [PubMed: 17229950]
2. McCormack VA, dos Santos Silva I (2006) Breast density and parenchymal patterns as markers of breast cancer risk: a meta-analysis. Cancer Epidemiol Biomarkers Prev 15:1159–1169 [PubMed: 16775176]
3. Tagliafico A, Tagliafico G, Astengo D et al. (2012) Mammographic density estimation: one-to-one comparison of digital mammography and digital breast tomosynthesis using fully automated software. Eur Radiol 22:1265–1270 [PubMed: 22358426]

4. Shepherd JA, Malkov S, Fan B, Laidevant A, Novotny R, Maskarinec G (2008) Breast density assessment in adolescent girls using dual-energy X-ray absorptiometry: a feasibility study. Cancer Epidemiol Biomarkers Prev 17:1709–1713 [PubMed: 18628421]
5. Lee NA, Rusinek H, Weinreb J et al. (1997) Fatty and fibroglandular-tissue volumes in the breasts of women 20-83 years old: Comparison of X-ray mammography and computer-assisted MR imaging. American Journal of Roentgenology 168:501–506 [PubMed: 9016235]
6. Blackmore KM, Dick S, Knight J, Lilge L (2008) Estimation of mammographic density on an interval scale by transillumination breast spectroscopy. J Biomed Opt 13:064030 [PubMed: 19123676]
7. Chen JH, Gulsen G, Su MY (2015) Imaging Breast Density: Established and Emerging Modalities. Transl Oncol 8:435–445 [PubMed: 26692524]
8. Bansal GJ, Kotugodella S (2014) How does semi-automated computer-derived CT measure of breast density compare with subjective assessments to assess mean glandular breast density, in patients with breast cancer? British Journal of Radiology 87
9. Moon WK, Lo CM, Goo JM et al. (2014) Quantitative analysis for breast density estimation in low dose chest CT scans. J Med Syst 38:21 [PubMed: 24643751]
10. Geeraert N, Klausz R, Cockmartin L, Muller S, Bosmans H, Bloch I (2014) Comparison of volumetric breast density estimations from mammography and thorax CT. Physics in Medicine and Biology 59:4391–4409 [PubMed: 25049219]
11. Salvatore M, Margolies L, Kale M et al. (2014) Breast density: comparison of chest CT with mammography. Radiology 270:67–73 [PubMed: 24126363]
12. Chen JH, Chan SW, Lu NH et al. (2016) Opportunistic Breast Density Assessment in Women Receiving Low-dose Chest Computed Tomography Screening. Academic Radiology 23:1154–1161 [PubMed: 27283069]
13. D'Orsi CJ, Sickles EA, Morris EA, eds. (2013) Breast imaging reporting and data system: ACR-BI-RADS-breast imaging atlas, 5th. American College of Radiology, Reston, VA
14. Pohl KM, Bouix S, Nakamura M et al. (2007) A hierarchical algorithm for MR brain image parcellation. Ieee Transactions on Medical Imaging 26:1201–1212 [PubMed: 17896593]
15. Zhou X-H, Obuchowski NA, McClish DK (2002) Statistical Methods in Diagnostic Medicine. John Wiley & Sons, Inc., New York
16. Lin LI (1989) A Concordance Correlation-Coefficient to Evaluate Reproducibility. Biometrics 45:255–268 [PubMed: 2720055]
17. Bland JM, Altman DG (1986) Statistical methods for assessing agreement between two methods of clinical measurement. Lancet 1:307–310 [PubMed: 2868172]
18. Cohen J (1968) Weighted Kappa - Nominal Scale Agreement with Provision for Scaled Disagreement or Partial Credit. Psychological Bulletin 70:213-& [PubMed: 19673146]
19. Kerlikowske K, Cook AJ, Buist DS et al. (2010) Breast cancer risk by breast density, menopause, and postmenopausal hormone therapy use. J Clin Oncol 28:3830–3837 [PubMed: 20644098]
20. Pettersson A, Graff RE, Ursin G et al. (2014) Mammographic density phenotypes and risk of breast cancer: a meta-analysis. J Natl Cancer Inst 106
21. Kuchiki M, Hosoya T, Fukao A (2010) Assessment of Breast Cancer Risk Based on Mammary Gland Volume Measured with CT. Breast Cancer (Auckl) 4:57–64 [PubMed: 21151862]
22. Boyd N, Martin L, Chavez S et al. (2009) Breast-tissue composition and other risk factors for breast cancer in young women: a cross-sectional study. Lancet Oncology 10:569–580 [PubMed: 19409844]
23. Denholm R, De Stavola B, Hipwell JH et al. (2016) Pre-natal exposures and breast tissue composition: findings from a British pre-birth cohort of young women and a systematic review. Breast Cancer Res 18:102 [PubMed: 27729066]
24. Sharma N, Aggarwal LM (2010) Automated medical image segmentation techniques. J Med Phys 35:3–14 [PubMed: 20177565]
25. Abramson RG, Burton KR, Yu JP et al. (2015) Methods and challenges in quantitative imaging biomarker development. Academic Radiology 22:25–32 [PubMed: 25481515]

26. Sprague BL, Conant EF, Onega T et al. (2016) Variation in Mammographic Breast Density Assessments Among Radiologists in Clinical Practice: A Multicenter Observational Study. Ann Intern Med 165:457–464 [PubMed: 27428568]

27. Horwood AC, Hogan SJ, Goddard PR, Rossiter J (2001) Image normalization, a basic requirement for computer-based automatic diagnostic applications. SemanticScholar; https://pdfs.semanticscholar.org/af1b/f1e6666a2561d9424a97a7a749541aeb6452.pdf?_ga=2.20893880.1876950350.1529958992-1664825032.1529958992

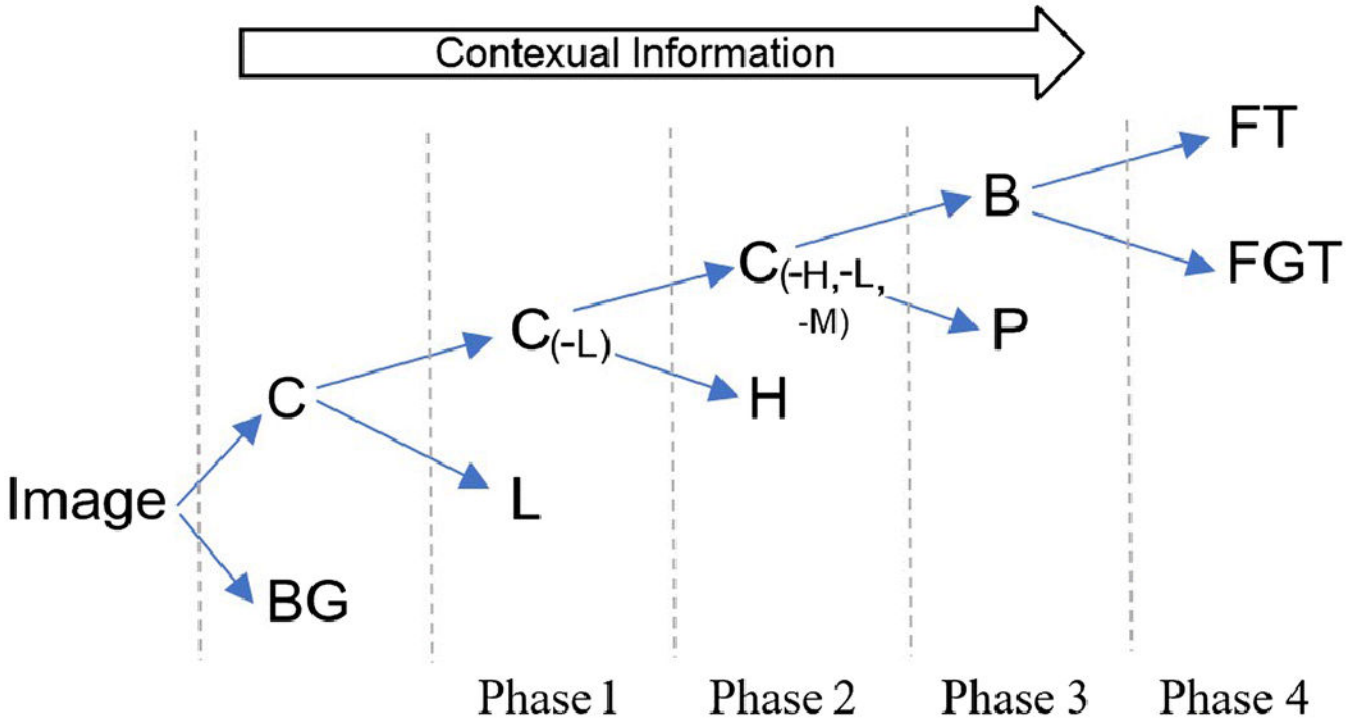

Figure 1. Illustration of the different phases for segmenting chest CT scans.

The system identifies and segments each structure in a different phase while passing contextual information to the next phase. BG = background; C = chest; L = lungs; $C_{(-L)}$ = chest region after eliminating the lungs; H = heart; $C_{(-H, -L, -M)}$ = chest region after eliminating the heart, lungs, and muscle; B = breast; P = pectoral muscle; FT = fatty component of the breast; and FGT = fibroglandular tissue.

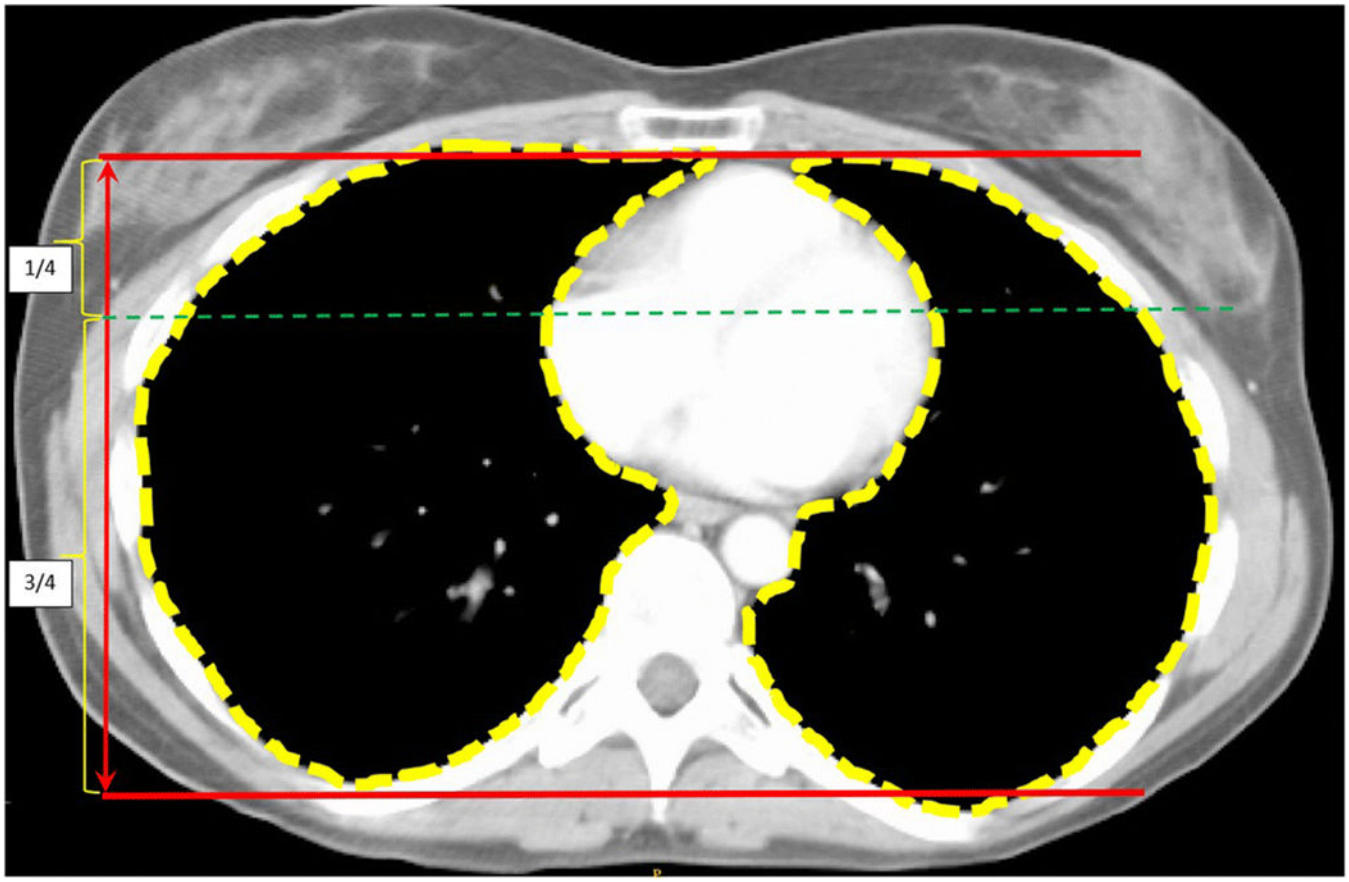

Figure 2. Construction of the horizontal boundary marking the anterior chest area.
The horizontal boundary (green dashed line) is drawn at approximately ¼ of the total vertical length of the lungs.

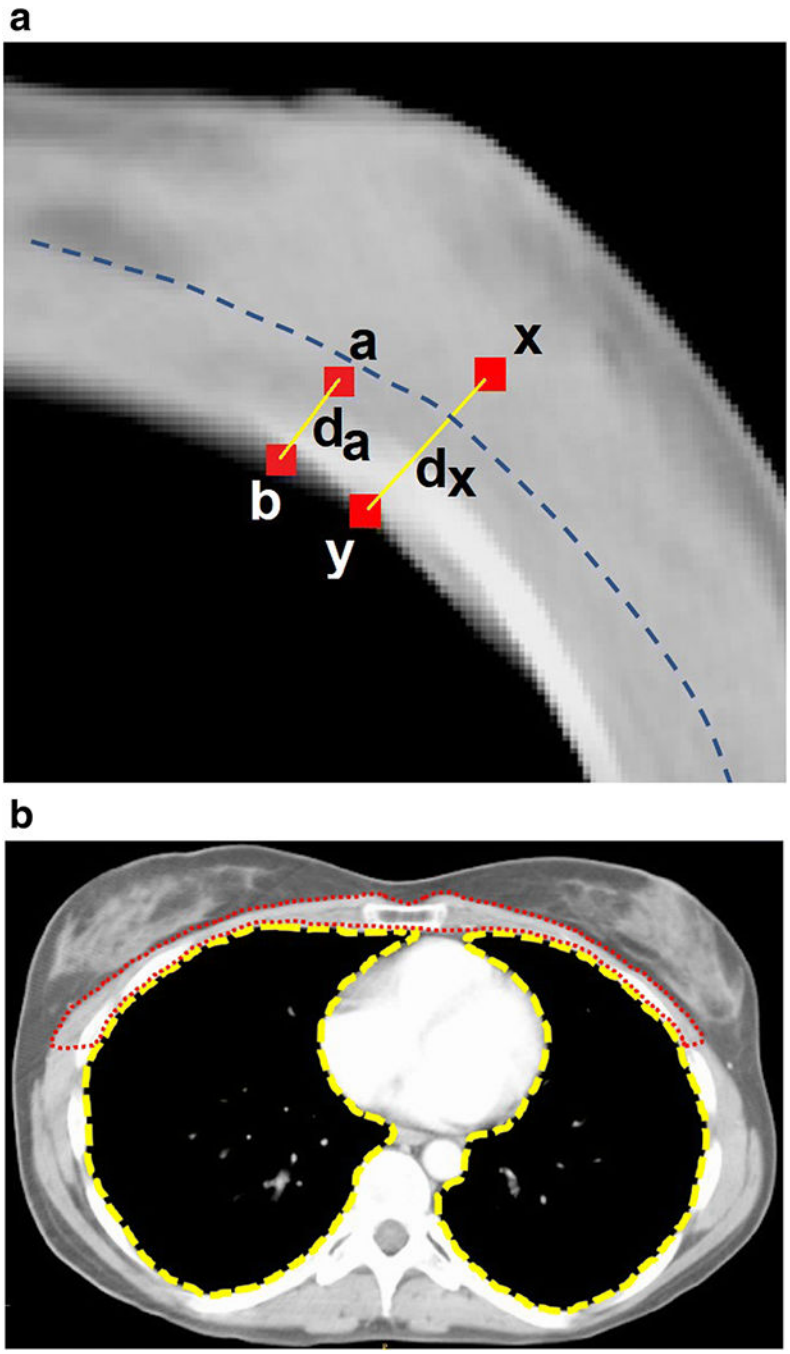

Figure 3.

(a) The distance offset feature. The Euclidian distance between pixel *x* and *y* is d_x, while the Euclidian distance between pixels *a* and *b* is d_a. Both *y* and *b* are lung boundary pixels. Since d_x is larger than d_a, *a* has a higher chance of belonging to pectoral muscle than *x*. The dashed line indicates the proposed boundary of pectoral muscle. Although fibroglandular breast tissue may share a boundary with pectoral muscle, and the gray level intensity of pixel *x* may be similar to the gray level intensity of pectoral muscle pixels, the chance of pixel *x* belonging to pectoral muscle is still conceptually low because of the higher value for d_x. **(b)**

Lungs and pectoral muscle segmentation. The dashed yellow line indicates the boundary of the lungs. The dotted red line indicates boundary of pectoral muscle.

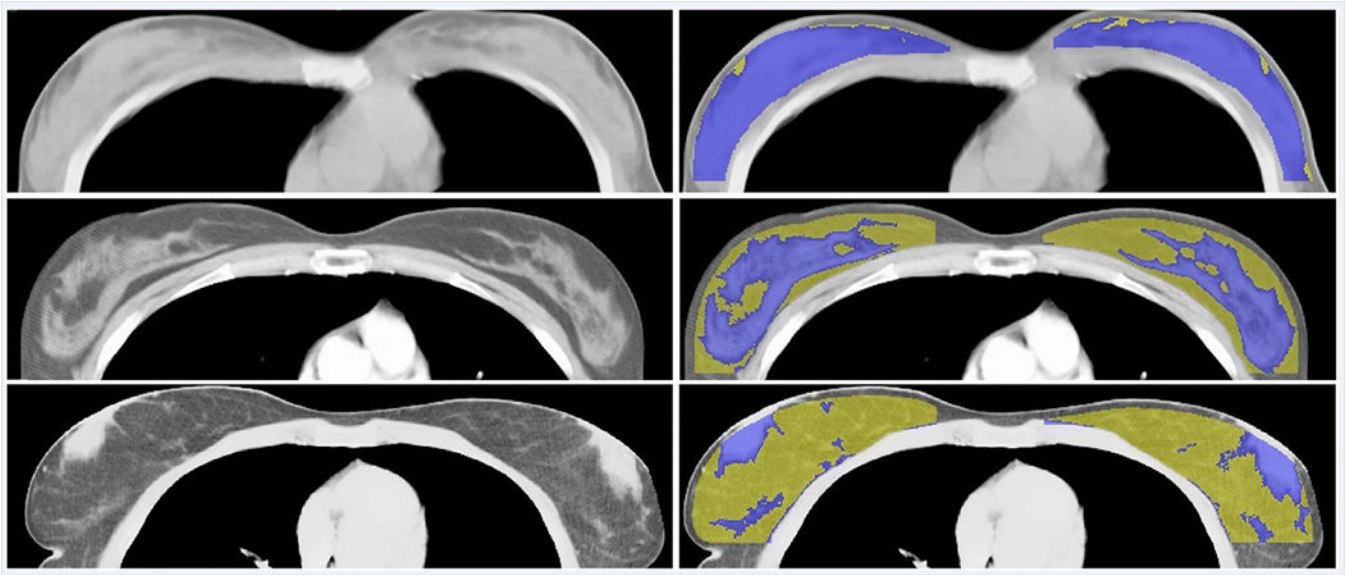

Figure 4. Sample output from the algorithm.
Fibroglandular tissue is depicted in blue and fatty tissue in yellow.

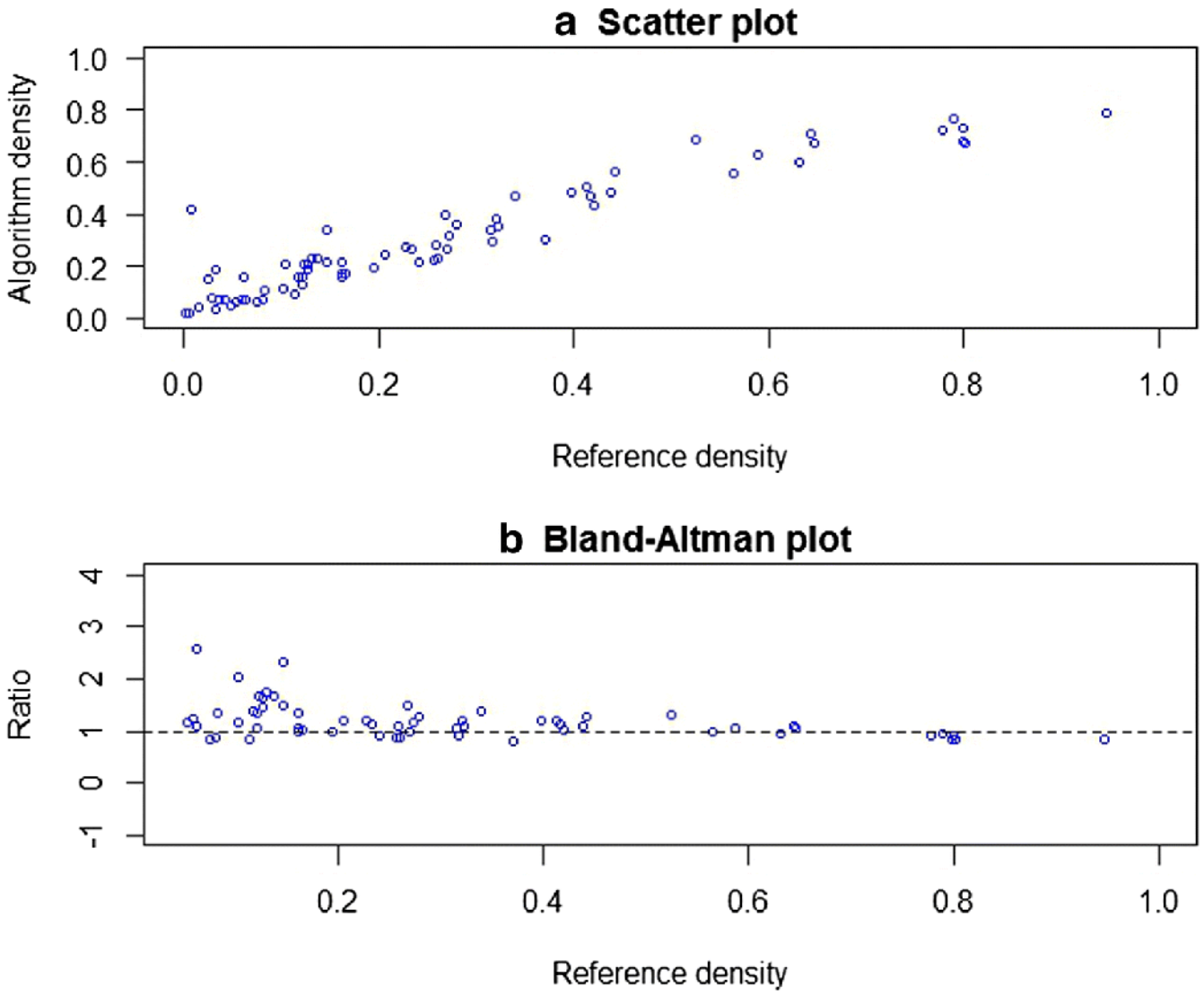

Figure 5. Agreement of percent breast density estimate between the algorithm and reference standard.

(a) Scatter plot of the percent density estimates from the algorithm and the reference standard data, (b) For images with percent density > 5% in the reference standard data, shown is the Bland-Altman plot of the ratio of the algorithm's breast density measurements relative to the breast density measurements from the reference data. The black dashed line corresponds to where there is no difference between the two measurements (i.e. ratio = 1).

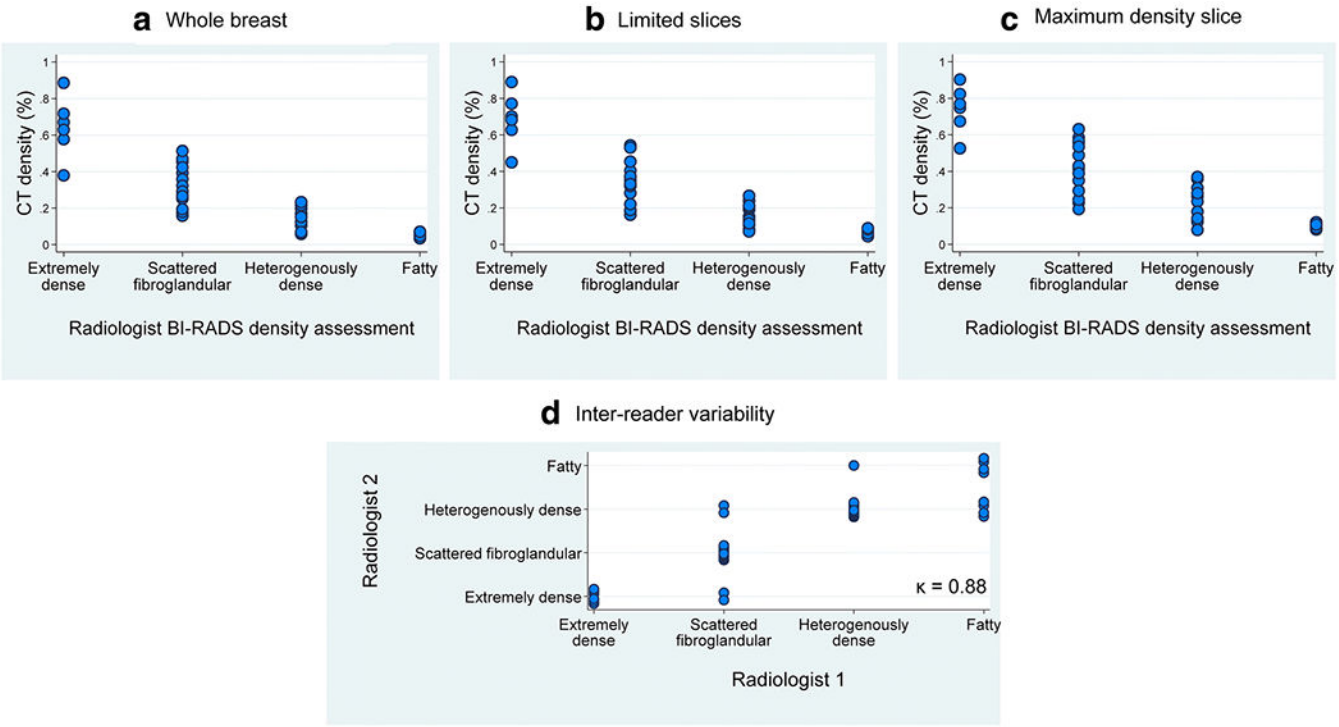

Figure 6. Agreement of algorithm's categorical percent breast density estimate with radiologist's subjective ACR BI-RADS assessment.

Shown in (a) – (c) are automated CT density measurements constructed three different ways: (a) using all slices in the identied breast region, (b) limiting the calculation to the slice with the highest density and the 10 neighboring slices, and (c) limiting the calculation to the slice with the highest density, (d) Inter-reader variability using subjective ACR BI-RADS assessments of chest CT scans.

Table 1.

Agreement between subjective breast density assessments from chest CT and mammography using ACR BI-RADS breast density categories.

	Kappa*	95% CI
Intraobserver variability (chest CT-mammography)		
Reader 1	0.87	(0.76, 0.91)
Reader 2	0.82	(0.71, 0.90)
Interobserver variability		
Mammography	0.85	(0.72, 0.92)
Chest CT	0.88	(0.81, 0.98)

*Estimated using a weighted kappa with quadratic weights to give more weight to differences that are further apart.